Ultrafast transition between exciton phases in van der Waals heterostructures

P. Merkl[1], F. Mooshammer[1], P. Steinleitner[1], A. Girnghuber[1], K.-Q. Lin[1], P. Nagler[1], J. Holler[1], C. Schüller[1], J. M. Lupton[1], T. Korn[1,3], S. Ovesen[2], S. Brem[2], E. Malic[2]* and R. Huber[1]*

Heterostructures of atomically thin van der Waals bonded monolayers have opened a unique platform to engineer Coulomb correlations, shaping excitonic[1-3], Mott insulating[4] or superconducting phases[5,6]. In transition metal dichalcogenide heterostructures[7], electrons and holes residing in different monolayers can bind into spatially indirect excitons[1,3,8-11] with a strong potential for optoelectronics[11,12], valleytronics[1,3,13], Bose condensation[14], superfluidity[14,15] and moiré-induced nanodot lattices[16]. Yet these ideas require a microscopic understanding of the formation, dissociation and thermalization dynamics of correlations including ultrafast phase transitions. Here we introduce a direct ultrafast access to Coulomb correlations between monolayers, where phase-locked mid-infrared pulses allow us to measure the binding energy of interlayer excitons in WSe_2/WS_2 heterobilayers by revealing a novel 1s–2p resonance, explained by a fully quantum mechanical model. Furthermore, we trace, with subcycle time resolution, the transformation of an exciton gas photogenerated in the WSe_2 layer directly into interlayer excitons. Depending on the stacking angle, intra- and interlayer species coexist on picosecond scales and the 1s–2p resonance becomes renormalized. Our work provides a direct measurement of the binding energy of interlayer excitons and opens the possibility to trace and control correlations in novel artificial materials.

In monolayers of transition metal dichalcogenides (TMDs), the confinement of electronic motion into two dimensions and the suppression of dielectric screening facilitate an unusually strong Coulomb interaction[17-20]. This gives rise to excitons with giant binding energies of several hundred meV (ref. [17]), small Bohr radii[18] and ultrashort radiative lifetimes[19]. When two monolayers are brought into contact with type-II band alignment, the conduction band minimum and the valence band maximum are located in two different layers[7]. Owing to their proximity, electron–hole (e–h) pairs in adjacent monolayers are still subject to strong mutual Coulomb attraction. Interband photoluminescence combined with theory has, indeed, provided evidence of interlayer excitons[8,21-23]. Because the composite electron and hole wavefunctions overlap only weakly in space, these excitons are long-lived—a key asset for future applications[1,3,14-16,24]. However, the weak coupling to light renders these quasiparticles inaccessible to interband absorption spectroscopy. The binding energies of interlayer excitons, which depend sensitively on the delocalization of the electronic wavefunctions over the heterostructure[23], have thus not been measured. Signatures of the ultrafast interlayer charge transfer have been studied by interband spectroscopy[8,21], but these techniques cannot measure Coulomb correlations or the formation of interlayer excitons on the intrinsic ultrashort timescales.

Meanwhile, phase-locked electromagnetic pulses in the terahertz (THz) and mid-infrared (MIR) range have directly accessed ultrafast low-energy excitations such as plasmons, phonons or correlation-induced energy gaps[25-28]. By probing the internal 1s–2p resonance, pre-existing exciton populations have been studied, even if interband selection rules render them optically dark[19,20,26,27]. Whereas THz and MIR pulses have unveiled excitonic correlations in quantum wells[26], perovskites[27] and monolayer TMDs[19,20], excitons in TMD hetero-bilayers have not been resolved. As the library of two-dimensional van der Waals materials is rapidly growing[24], and exciting new phases may be tailored artificially[1-5], a precise quantitative understanding of Coulomb correlations between monolayers is vital.

Here we exploit near-infrared pump–MIR probe spectroscopy to measure the binding energy of spatially indirect excitons and the ultrafast transition of intralayer excitons into an interlayer insulating phase in WSe_2/WS_2 bilayers (Fig. 1a), depending on the stacking angle. The samples are manufactured by mechanical exfoliation of individual monolayers and subsequent deterministic transfer onto a diamond substrate (see Methods). In a first sample, monolayers of WSe_2 and WS_2 overlap in a large patch (Fig. 1b) with a diameter of ~80 μm with a stacking angle of $\theta = 5° \pm 3°$ (see Methods). In the overlap area, the photoluminescence at the 1s A exciton lines of the bare monolayers is quenched (Fig. 1c), attesting to good contact between the monolayers. We also prepared a reference monolayer of WSe_2 on a diamond substrate, covered with hexagonal boron nitride (hBN) (Supplementary Fig. 1a). This structure features a spatially uniform photoluminescence of the WSe_2 1s A exciton (Supplementary Fig. 1b).

We first prove that MIR probing can unequivocally distinguish between spatially direct and indirect excitons. A 100 fs near-infrared (NIR) pump pulse, centred at a photon energy of 1.67 eV (Supplementary Fig. 2a) resonantly injects 1s A excitons into the WSe_2 monolayer (Fig. 1d). Because this energy lies well below the lowest interband resonance of WS_2 and hBN, we do not directly excite these materials. After a variable delay time t_{pp}, a phase-locked few-cycle MIR pulse (Fig. 1d, red waveform; centre frequency, 22 THz; spectral width, 19 THz; see also Supplementary Fig. 2b,c) is transmitted through the sample. The interaction with the photoinjected e–h pairs imparts a characteristic change on the amplitude and phase of the MIR waveform, which we directly record by electro-optic sampling[19,20,25-28]. A Fourier transform and a Fresnel analysis allow us to extract the full dielectric response of the non-equilibrium system[25,26] (see Methods). The pump-induced
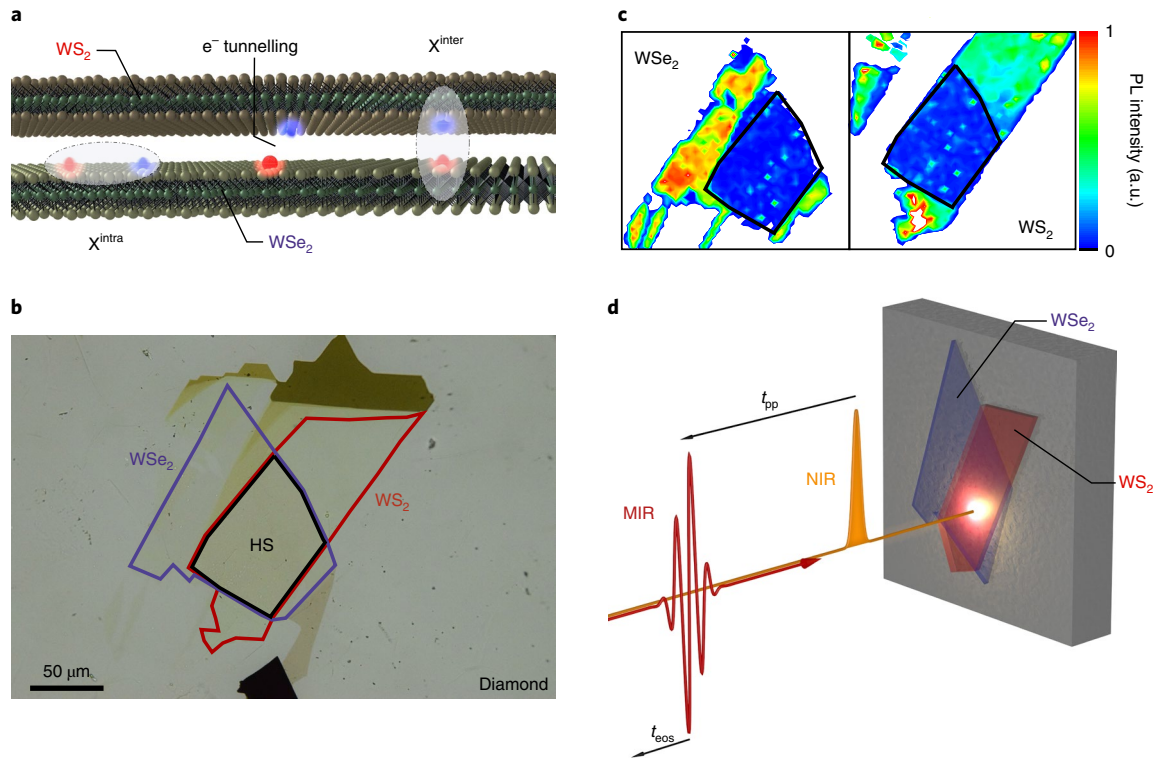
Fig. 1 | NIR pump–MIR probe spectroscopy of a WSe$_2$/WS$_2$ hetero-bilayer. a, Artistic illustration of the electron tunnelling process and interlayer exciton formation out of intralayer excitons in a WSe$_2$/WS$_2$ heterostructure. **b,** Optical microscope image of the heterostructure. The purple frame indicates the WSe$_2$ monolayer, which is covered by a WS$_2$ monolayer (red frame). The heterostructure (HS) is formed in the overlap region (black frame). **c,** Micro-photoluminescence intensity map at the photon energy of the interband resonance of the 1s A exciton of WSe$_2$ (left) and WS$_2$ (right) when excited by a continuous-wave (c.w.) laser at a wavelength of 532 nm. All experiments were performed at room temperature. **d,** Time-resolved NIR pump–MIR probe spectroscopy of the heterostructure, which is van der Waals bonded on a diamond substrate. The 100 fs NIR pump pulse (orange) resonantly injects 1s A excitons into the WSe$_2$ monolayer. The ultrabroadband MIR probe pulse (red waveform) samples the dielectric response of the heterostructure.

changes of the real parts of the optical conductivity $\Delta\sigma_1$ and of the dielectric function $\Delta\varepsilon_1$ describe the absorptive and inductive responses, respectively.

Coulomb correlations leave characteristic fingerprints in the dielectric response. At $t_{pp} = 175$ fs, the response in the reference sample is dominated by a maximum in $\Delta\sigma_1$ (Fig. 2a) and a corresponding zero crossing in $\Delta\varepsilon_1$ (Fig. 2b) at a photon energy of 144 ± 6 meV. This resonance marks the recently discovered $1s$–$2p$ transition of excitons within the WSe$_2$ monolayer[19]. The energy is slightly red-shifted with respect to the value of a bare WSe$_2$ monolayer[19] due to dielectric screening by the hBN cover layer[20]. Most remarkably, an analogous experiment with the WSe$_2$/WS$_2$ heterostructure yields a dramatically different result (Fig. 2c,d). At a delay time of 5.1 ps after photoinjection of excitons in the WSe$_2$ monolayer, the strong resonance at an energy of 144 meV is absent. Instead, a maximum in $\Delta\sigma_1$ (Fig. 2c) and a dispersive feature in $\Delta\varepsilon_1$ (Fig. 2d) at an energy of 67 ± 6 meV dominate the response. This signature, which is spectrally far below the known internal $1s$–$2p$ resonances of intralayer excitons (see Methods) and far above the phonon frequencies of the TMD materials used here (Supplementary Fig. 2d), is characteristic of interlayer excitons, as shown next.

Owing to the type-I band alignment between WSe$_2$ and hBN (Fig. 2b, inset), excitons photoinjected in the reference sample remain within WSe$_2$ (ref. [20]). The staggered band alignment in the WSe$_2$/WS$_2$ bilayer (Fig. 2d, inset), in contrast, should enable interlayer electron tunnelling[29]. This process competes with the radiative recombination of the intralayer excitons[19], quenching the photoluminescence of the WSe$_2$ monolayer[8] (Fig. 1c). The Coulomb attraction

between electrons and holes remains strong even if they are spatially separated in neighbouring monolayers. The eigenenergies E_b and wavefunctions φ_q of the bound states are obtained by solving the Wannier equation

$$\frac{\hbar^2 q^2}{2\mu}\varphi_q - \sum_k V_{k-q}\varphi_k = E_b\varphi_q \qquad (1)$$

Here, μ is the reduced mass, and the effective 2D Coulomb potential V_k is derived by generalizing the Keldysh potential of the monolayer case to heterostructures and solving the Poisson equation self consistently. With literature values for the interlayer distance and the relevant dielectric constants, we compute a $1s$–$2p$ energy separation of 147 ± 3 meV and 69 ± 5 meV (Fig. 2e,f) for the reference sample and the WSe$_2$/WS$_2$ bilayer (see Methods), respectively, which coincide very well with the measured resonances of Fig. 2a–d. The $1s$ and $2p$ wavefunctions are qualitatively similar for intra- (Fig. 2e) and interlayer (Fig. 2f) species, and the dipolar nature of the $2p$ wavefunctions warrants an in-plane orientation of the $1s$–$2p$ transition dipole for both cases. Because these resonances carry by far the largest oscillator strength of all intra-excitonic transitions they are expected to dominate the MIR spectra, as indeed is observed experimentally. The excellent agreement between experiment and theory allows us to quantify the corresponding binding energy of the interlayer excitons in the WSe$_2$/WS$_2$ bilayer under these conditions as 126 ± 7 meV (see Methods and Supplementary Section 3), substantially exceeding the thermal energy at room temperature.
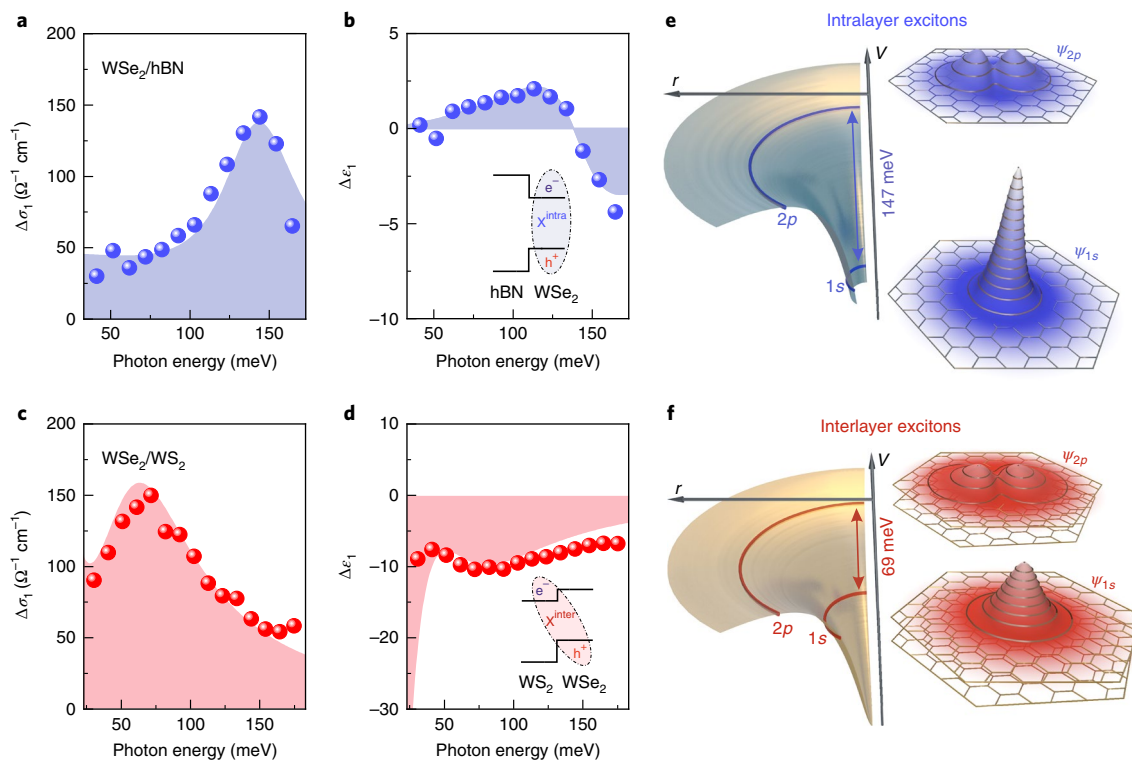
Fig. 2 | Dielectric response of intra- and interlayer excitons and excitonic wavefunctions. a–d, Pump-induced changes of the real parts of the optical conductivity $\Delta\sigma_1$ (**a,c**), and the dielectric function $\Delta\varepsilon_1$ (**b,d**), as a function of the photon energy. The pump-induced dielectric response of the reference WSe$_2$/hBN structure is shown for $t_{pp} = 175$ fs (**a,b**). For the $\theta = 5°$ WSe$_2$/WS$_2$ heterostructure (**c,d**), the response is depicted at $t_{pp} = 5.1$ ps. The blue and red spheres denote the experimental data of the photoexcited heterostructures at a pump fluence of $\Phi = 27\,\mu$J cm^{-2}. Shaded areas represent the three-fluid model fitting the experimental data, as discussed in the main text. Inset in **b**, schematic band alignment for the WSe$_2$/hBN heterostructure hosting intralayer excitons X^{intra} in the WSe$_2$ monolayer. Inset in **d**, band alignment for the WSe$_2$/WS$_2$ heterostructure supporting the formation of interlayer excitons X^{inter}. **e**, Intralayer Coulomb potential and wavefunctions of the 1s and 2p intralayer excitons in real space. **f**, Interlayer Coulomb potential and wavefunctions of the 1s and 2p interlayer excitons in real space.

Next, we utilize the hallmark MIR resonances to track the dynamics of Coulomb correlations. By repeating the NIR pump–MIR probe experiment for variable delay times t_{pp}, we map out the time evolution of $\Delta\sigma_1$ of the WSe$_2$/WS$_2$ heterostructure (Fig. 3a; see Supplementary Fig. 4e for $\Delta\varepsilon_1$). $\Delta\sigma_1$ sets on sharply at $t_{pp} = 0$ ps. Only 100 fs later, a broad maximum at an energy of ~150 meV indicates the presence of intralayer excitons in WSe$_2$. Already at this time, a broad shoulder at ~67 meV attests to the formation of interlayer excitons. Within the subsequent 100 fs, the spectral weight shifts from the intra- to the interlayer resonance, as seen at $t_{pp} = 0.2$ ps. Subsequently, the intralayer resonance disappears completely while the spectral weight of the interlayer exciton resonance continues to grow until $t_{pp} = 5.1$ ps. This dynamics is faithfully reproduced by a microscopic model (Fig. 3c) based on the density matrix formalism discussed in more detail below (see also Methods). Our experimental data thus directly resolve the transformation of intralayer excitons into interlayer bound states in the time domain. For $t_{pp} > 5.1$ ps, $\Delta\sigma_1$ decreases as the interlayer exciton population decays (Fig. 3a). Intriguingly, the exciton resonance is blueshifted by ~20 meV at $t_{pp} = 50$ ps.

To test the influence of the stacking angle, we repeated the pump–probe experiment under identical conditions with a comparable WSe$_2$/WS$_2$ bilayer featuring $\theta = 27° \pm 3°$ (Supplementary Fig. 1c,d). The dynamics of $\Delta\sigma_1$ (Fig. 3b; see Supplementary Fig. 4f for $\Delta\varepsilon_1$) is similar to that in Fig. 3a, with two exceptions: (1) the spectral weight in the vicinity of the intralayer exciton resonance remains observable at $t_{pp} = 5.1$ ps; (2) the peculiar blueshift of the interlayer exciton resonance at $t_{pp} = 50$ ps does not occur for $\theta = 27°$.

For a quantitative discussion, we fit the MIR response with a phenomenological three-fluid model, which accounts for the two Lorentzian resonances of inter- and intralayer 1s–2p transitions and includes a contribution of excited interlayer exciton states as discussed below (see also Methods). The energies and dipole moments of the exciton resonances are adopted from the above theory whereas the inter- and intralayer exciton densities, n_{inter} and n_{intra}, as well as the spectral weight of the excited interlayer exciton states, are freely varied. The requirement to simultaneously reproduce the spectra of both $\Delta\sigma_1$ and $\Delta\varepsilon_1$ (Fig. 3a,b and Supplementary Fig. 4b,c,e,f) sets narrow boundaries for acceptable exciton densities (Fig. 4a,b). We observe that n_{intra} (Fig. 4a) peaks immediately after the pump pulse, at $t_{pp} = 100$ fs, for both heterostructures. The subsequent decay, however, is significantly slower in the strongly twisted bilayer ($\theta = 27°$) than for $\theta = 5°$, where a notable decay occurs within less than 0.2 ps. Furthermore, the maximum of n_{intra} is larger for $\theta = 27°$, even though the pump fluence is identical in both structures. This confirms that, for $\theta = 5°$, tunnelling into the WS$_2$ layer occurs on the same timescale as the photogeneration of intralayer excitons. Accordingly, n_{inter} (Fig. 4b) rises quickly within the initial few hundred femtoseconds after optical excitation and levels off at $t_{pp} = 5.1$ ps. The maximum observed for $\theta = 5°$ is approximately twice as large as in the more twisted bilayer, again attesting to a strongly enhanced tunnelling rate at $\theta = 5°$. The MIR response of both hetero-bilayers can only be fitted satisfactorily if additional spectral weight below the observed frequency window is included. Such a response can be caused by unbound e–h pairs or excited-state absorption of bound states[30], both of which we
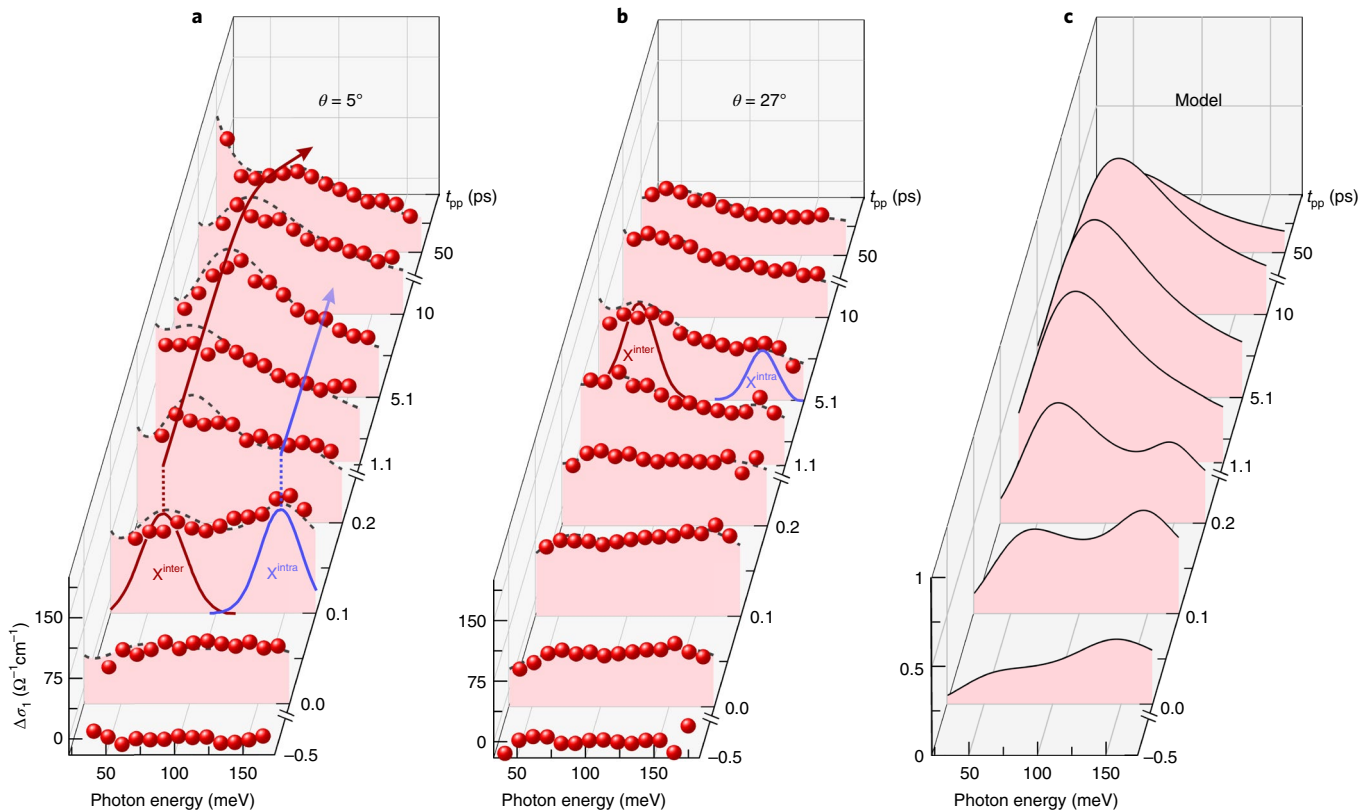
Fig. 3 | Temporal evolution of the dielectric response in experiment and theory. a,b, Pump-induced change of the optical conductivity $\Delta\sigma_1$ of the photoexcited heterostructures as a function of the photon energy at selected delay times t_{pp} (pump fluence, $\Phi = 27\,\mu J\,cm^{-2}$), for almost aligned ($\theta = 5°$) (**a**) and misaligned ($\theta = 27°$) (**b**) heterostructures. Red spheres indicate experimental data. Dashed curves present phenomenological three-fluid model fitting of the data, as discussed in the main text. The red and blue Gaussian curves in **a** and **b** indicate the spectral positions of the inter- and intralayer exciton absorption, respectively. **c**, Normalized pump-induced change of the optical conductivity $\Delta\sigma_1$ modelled by the microscopic theory discussed in the main text, for $\theta = 5°$ and the delay times interrogated in the experiment.

phenomenologically account for in the form of a low-frequency Lorentz oscillator. From the temporal evolution of this component (Supplementary Fig. 5b,d,f) we estimate the density of unbound charge carriers to always remain at least a factor of 7 below the total density of e–h pairs, suggesting no dominant intermediate plasma phase during the formation of interlayer excitons.

The observed dynamics is well described by a microscopic model as illustrated in Fig. 4c. Because electrons and holes in interlayer excitons reside in different layers, the lattice mismatch between WSe_2 and WS_2 leads to a momentum displacement between the intra- and interlayer exciton dispersion (grey shaded parabolas). After photoinjection at a vanishing centre-of-mass momentum ($Q = 0$), $1s$ intralayer excitons spread out in reciprocal space via phonon scattering (Fig. 4c, orange arrow), while the entire ensemble is traced by its $1s$–$2p$ transition (Fig. 4c, blue arrows). The electrons can tunnel into the WS_2 layer under conservation of energy, which is most efficient at the intersection points of the inter- and intralayer dispersion relations, where also the in-plane momentum Q is conserved. Intralayer excitons may be transformed into interlayer unbound or bound states with a broad range of possible orbital quantum numbers. These quasiparticles subsequently relax towards the $1s$ interlayer state (Fig. 4c, green arrows), leading to the characteristic $1s$–$2p$ absorption (Fig. 4c, red arrows).

To model this scenario, we compute the temporal evolution of incoherent exciton densities for intra- and interlayer populations, including tunnelling, phonon scattering, radiative decay, non-radiative decay and intra-excitonic relaxation (see Methods). These simulations

reproduce the spectral shape and the temporal evolution of $\Delta\sigma_1$ (Fig. 3c) as well as the dynamics of the intra- and interlayer exciton density, for $\theta = 5°$ and 27°, at all $t_{pp} < 50\,ps$ (Fig. 4a,b, solid/dashed curves). Interestingly, direct tunnelling into the $1s$ interlayer state is the most efficient quantum channel with a branching ratio of 54% (see Methods). Moreover, our model shows that the measurable difference of interlayer tunnelling rates of $\Gamma = (200\,fs)^{-1}$ at $\theta = 5°$ and $\Gamma = (1.2\,ps)^{-1}$ at $\theta = 27°$ is primarily caused by the momentum offset of inter- and intralayer exciton dispersions (see Methods).

Apart from the ultrafast formation of interlayer excitons, θ also strongly influences their long-term dynamics, where a blueshift of the $1s$–$2p$ resonance occurs in the nearly aligned hetero-bilayer (Fig. 3a, for $t_{pp} = 50\,ps$). We suggest that this phenomenon could be caused by lateral quantum confinement of excitons[16] (Supplementary Section 6). The slight lattice mismatch between WSe_2 and WS_2 entails a moiré pattern of alternating AA and AB stacking (Fig. 4d), which induces a periodic modulation of the potential energy experienced by interlayer excitons[16] (Fig. 4e). Owing to their small Bohr radii, the interlayer excitons may be captured in areas with AB stacking as they cool down. The additional quantum confinement could explain the blueshift of the $1s$–$2p$ resonance for $t_{pp} = 50\,ps$ (Fig. 3a; see Methods).

This effect is even more pronounced in a third, precisely aligned hetero-bilayer with $\theta = 0 \pm 2°$ (Supplementary Fig. 1e,f), where the moiré period reaches its largest value of 9 nm, the potential energy modulation is maximal and interlayer excitons should be created with particularly small centre-of-mass momenta owing to the minimum momentum mismatch between intra- and interlayer excitons.
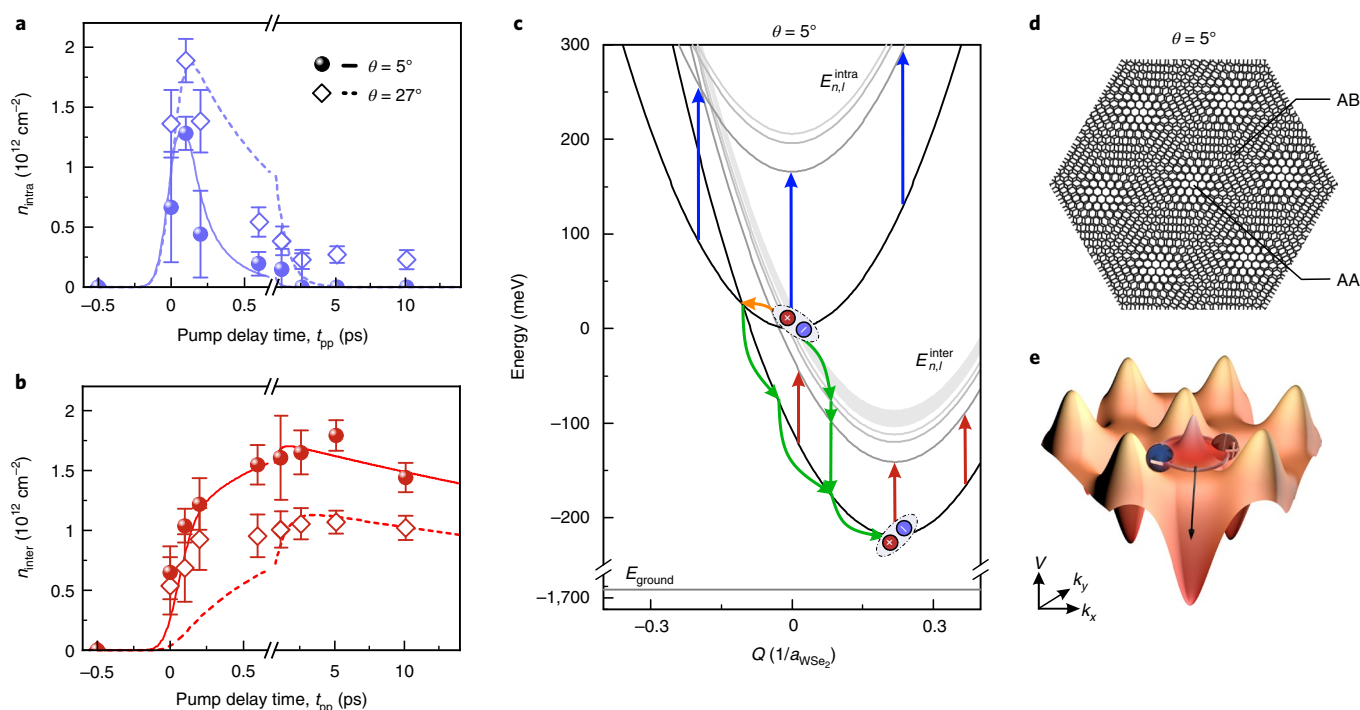
Fig. 4 | Ultrafast evolution of intra- and interlayer exciton densities and microscopic model. a,b, Intralayer (**a**) and interlayer (**b**) exciton density extracted by the fitting procedure of the data in Fig. 3a,b and Supplementary Fig. 4b,c,e,f as a function of the pump–probe delay time t_{pp} for the WSe$_2$/WS$_2$ heterostructures with $\theta = 5°$ (spheres) and $\theta = 27°$ (diamonds). The solid and dashed curves in **a** and **b** represent the result of the microscopic model discussed in the text, for $\theta = 5°$ and 27°, respectively. Error bars represent the 95% confidence interval of the fitting procedure. **c,** Dispersion $E_{n,l}$ of intra- and interlayer excitons in the two-particle picture, for $\theta = 5°$ and a number of quantum states characterized by the principle quantum number n and the orbital quantum number l. Black parabolas: 1s excitons; grey parabolas: excitons with $n > 1$. The blue (red) arrows represent the 1s–2p transition of intralayer (interlayer) excitons. Phonon scattering can spread the intralayer exciton population in momentum space (orange arrow). The cascades of green arrows indicate possible decay channels for intralayer excitons to form interlayer states. The origin of the energy scale is shifted to the 1s intralayer exciton state with vanishing centre-of-mass momentum Q in units of the reciprocal lattice constant of WSe$_2$, a_{WSe_2}. **d,** Superposition of the two monolayer lattices for a twist angle of $\theta = 5°$, forming a moiré pattern in real space. Bright regions correspond to AA stacking, whereas darker regions correspond to AB stacking. **e,** The real-space moiré pattern induces a local variation of the potential energy V, whose period and amplitude strongly depend on the stacking angle. Small twist angles facilitate the localization of 1s interlayer excitons, giving rise to a blueshift of the 1s–2p resonance due to increased quantum confinement.

Indeed for this structure, the interlayer exciton resonance starts out at a relatively high photon energy of 83 ± 6 meV and does not shift any further for later delay times (Supplementary Fig. 4a,d), suggesting that interlayer excitons may be efficiently captured in confined states already at early delay times t_{pp}. In contrast, the moiré period of 0.6 nm for $\theta = 27°$ (Supplementary Fig. 1g), which is substantially smaller than the exciton Bohr radius (Supplementary Fig. 1h), will not allow excitons to be efficiently captured, as is seen by the absence of a transient blueshift in Fig. 3b.

In conclusion, the direct study of interlayer Coulomb correlations allows us to measure the large binding energies of spatially indirect excitons. By probing all excitons, independently of their centre-of-mass momenta, spin orientation or interband selection rules, we discover an unexpectedly efficient ultrafast transition of spatially direct into indirect excitons without a pronounced intermediate plasma phase of unbound e–h pairs. The twist angle θ has a strong influence on the formation and cooling dynamics of interlayer excitons. While we extract a binding energy of 126 ± 7 meV for itinerant interlayer excitons, blueshifted 1s–2p resonances may be caused by quantum confinement within the moiré pattern. In the same spirit, observing Coulomb correlations and their ultrafast dynamics in the extensive library of van der Waals heterostructures opens a versatile playground for fundamental materials sciences and may become an invaluable help in searching for novel man-made equilibrium and hidden phases.

Online content

Any methods, additional references, Nature Research reporting summaries, source data, statements of data availability and associated accession codes are available at https://doi.org/10.1038/s41563-019-0337-0.

References

1. Rivera, P. et al. Valley-polarized exciton dynamics in a 2D semiconductor heterostructure. *Science* **351**, 688–691 (2016).
2. Ju, L. et al. Tunable excitons in bilayer graphene. *Science* **358**, 907–910 (2017).
3. Jin, C. et al. Imaging of pure spin-valley diffusion current in WS$_2$–WSe$_2$ heterostructures. *Science* **360**, 893–896 (2018).
4. Cao, Y. et al. Correlated insulator behaviour at half-filling in magic-angle graphene superlattices. *Nature* **556**, 80–84 (2018).
5. Cao, Y. et al. Unconventional superconductivity in magic-angle graphene superlattices. *Nature* **556**, 43–50 (2018).
6. Lee, J. J. et al. Interfacial mode coupling as the origin of the enhancement of T_c in FeSe films on SrTiO$_3$. *Nature* **515**, 245–248 (2014).
7. Gong, Y. et al. Vertical and in-plane heterostructures from WS$_2$/MoS$_2$ monolayers. *Nat. Mater.* **13**, 1135–1142 (2014).
8. Hong, X. et al. Ultrafast charge transfer in atomically thin MoS$_2$/WS$_2$ heterostructures. *Nat. Nanotechnol.* **9**, 682–686 (2014).
9. Rivera, P. et al. Observation of long-lived interlayer excitons in monolayer MoSe$_2$–WSe$_2$ heterostructures. *Nat. Commun.* **6**, 6242 (2015).

10. Arora, A. et al. Interlayer excitons in a bulk van der Waals semiconductor. *Nat. Commun.* **8**, 639 (2017).
11. Ross, J. S. et al. Interlayer exciton optoelectronics in a 2D heterostructure p–n junction. *Nano Lett.* **17**, 638–643 (2017).
12. Unuchek, D. et al. Room-temperature electrical control of exciton flux in a van der Waals heterostructure. *Nature* **560**, 340–344 (2018).
13. Baranowski, M. et al. Probing the interlayer exciton physics in a $MoS_2/MoSe_2/MoS_2$ van der Waals heterostructure. *Nano Lett.* **17**, 6360–6366 (2017).
14. Su, J.-J. & MacDonald, A. H. How to make a bilayer exciton condensate flow. *Nat. Phys.* **4**, 799–802 (2008).
15. Fogler, M. M., Butov, L. V. & Novoselov, K. S. High-temperature superfluidity with indirect excitons in van der Waals heterostructures. *Nat. Commun.* **5**, 4555 (2014).
16. Yu, H., Liu, G.-B., Tang, J., Xu, X. & Yao, W. Moiré excitons: from programmable quantum emitter arrays to spin–orbit-coupled artificial lattices. *Sci. Adv.* **3**, e1701696 (2017).
17. Ugeda, M. M. et al. Giant band gap renormalization and excitonic effects in a monolayer transition metal dichalcogenide semiconductor. *Nat. Mater.* **13**, 1091–1095 (2014).
18. Chernikov, A. et al. Exciton binding energy and nonhydrogenic Rydberg series in monolayer WS_2. *Phys. Rev. Lett.* **113**, 076802 (2014).
19. Poellmann, C. et al. Resonant internal quantum transitions and femtosecond radiative decay of excitons in monolayer WSe_2. *Nat. Mater.* **14**, 889–893 (2015).
20. Steinleitner, P. et al. Dielectric engineering of electronic correlations in a van der Waals heterostructure. *Nano Lett.* **18**, 1402–1409 (2018).
21. Chen, H. et al. Ultrafast formation of interlayer hot excitons in atomically thin MoS_2/WS_2 heterostructures. *Nat. Commun.* **7**, 12512 (2016).
22. Miller, B. et al. Long-lived direct and indirect interlayer excitons in van der Waals heterostructures. *Nano Lett.* **17**, 5229–5237 (2017).
23. Kunstmann, J. et al. Momentum-space indirect interlayer excitons in transition-metal dichalcogenide van der Waals heterostructures. *Nat. Phys.* **14**, 801–805 (2018).
24. Mounet, N. et al. Two-dimensional materials from high-throughput computational exfoliation of experimentally known compounds. *Nat. Nanotechnol.* **13**, 246–252 (2018).
25. Huber, R. et al. How many-particle interactions develop after ultrafast excitation of an electron-hole plasma. *Nature* **414**, 286–289 (2001).
26. Kaindl, R. A., Carnahan, M. A., Hägele, D., Lövenich, R. & Chemla, D. S. Ultrafast terahertz probes of transient conducting and insulating phases in an electron–hole gas. *Nature* **423**, 734–738 (2003).
27. Luo, L. et al. Ultrafast terahertz snapshots of excitonic Rydberg states and electronic coherence in an organometal halide perovskite. *Nat. Commun.* **8**, 15565 (2017).
28. Ulbricht, R., Hendry, E., Shan, J., Heinz, T. F. & Bonn, M. Carrier dynamics in semiconductors studied with time-resolved terahertz spectroscopy. *Rev. Mod. Phys.* **83**, 543 (2011).
29. Wang, K. et al. Interlayer coupling in twisted WSe_2/WS_2 bilayer heterostructures revealed by optical spectroscopy. *ACS Nano* **10**, 6612–6622 (2016).
30. Brem, S., Selig, M., Berghaeuser, G. & Malic, E. Exciton relaxation cascade in two-dimensional transition metal dichalcogenides. *Sci. Rep.* **8**, 8238 (2018).

Author contributions

R.H. and E.M. supervised the study. P.M., F.M., P.S., A.G. and R.H. carried out the experiments. P.S., P.M., F.M., A.G., K.-Q.L., P.N., J.H., C.S., J.M.L. and T.K. prepared and pre-characterized the large-area heterostructures. S.O., S.B. and E.M. carried out the theoretical modelling. All authors analysed the data, discussed the results and contributed to the writing of the manuscript.

Competing interests

The authors declare no competing interests.

Additional information

Supplementary information is available for this paper at https://doi.org/10.1038/s41563-019-0337-0.

Reprints and permissions information is available at www.nature.com/reprints.

Correspondence and requests for materials should be addressed to E.M. or R.H.

Publisher's note: Springer Nature remains neutral with regard to jurisdictional claims in published maps and institutional affiliations.

Methods

Sample fabrication and characterization. The TMD monolayers were fabricated via mechanical exfoliation[31]. Starting from the bulk single crystal, a thin flake of the material was exfoliated with Nitto-tape and placed on a viscoelastic poly-dimethyl-siloxane (PDMS) substrate. By gently lifting the tape, a single monolayer of the TMD was left on the substrate. The monolayer was pre-characterized under an optical microscope before being stamped onto a diamond substrate using a micro-positioning stage. This procedure could be repeated to stack multiple monolayers on top of each other while accurately aligning their position and twist angle θ with the translation stage. To confirm the structural integrity and contact of the heterostructure sample we recorded room-temperature micro-photoluminescence intensity maps of the individual monolayers after the fabrication of the heterostructure, excited by a c.w. laser at a wavelength of 532 nm. The angle θ was identified by tracing the characteristic cleavage edges along the armchair and zigzag directions of the monolayers spanning a 120° angle. Additionally, θ was confirmed for each heterostructure by polarization-resolved second harmonic generation[23,32]. For this, a linearly polarized Ti:sapphire laser was used to excite the monolayers, and the polarization component of the second harmonic, parallel to the polarization of the fundamental, was analysed. This gave direct access to the armchair directions of the monolayers and therefore the twist angle of the hetero-bilayer.

Ultrafast NIR pump–MIR probe spectroscopy. Figure 1d presents a schematic of the experimental set-up. A 100 fs pump pulse centred at an energy of 1.67 eV (Supplementary Fig. 2a) from a home-built Ti:sapphire laser amplifier resonantly injects 1s A excitons into the WSe$_2$ monolayer at a repetition rate of 400 kHz. Another part of the laser output generates phase-locked MIR probe pulses by optical rectification in a 10-μm-thick GaSe crystal. This probe pulse propagates through the photoexcited sample after a variable delay time t_{pp}. The MIR waveform and any changes induced by the sample are fully resolved by electro-optic sampling in a second GaSe crystal, as a function of the electro-optic sampling time t_{eos} (Supplementary Fig. 2b). The MIR probe pulse is centred at a frequency of 22 THz with a full-width at half-maximum (FWHM) of 19 THz (Supplementary Fig. 2c, black curve) and a spectral phase that is flat between 15 and 45 THz (Supplementary Fig. 2c, blue curve). Using serial lock-in detection, we recorded the electric field of the MIR probe pulse propagating through the unexcited and the photoexcited sample. This allowed us to determine the pump-induced change $\Delta E(t_{eos})$ of the MIR electric field as function of the detection time t_{eos}. Applying a transfer matrix formalism, we thus had access to the full complex-valued dielectric response function, characterized by $\Delta\sigma_1$ and $\Delta\varepsilon_1$. This technique is sensitive to bound and unbound e–h pair populations, irrespective of interband selection rules, and may thus interrogate optically dark and bright excitons[33].

Solution of the Wannier equation and effective 2D Coulomb potential. The excitonic binding energies and wavefunctions were obtained by finding the eigenenergies E_b, and eigenfunctions φ_q of the Wannier equation (see equation (1) in the main text). Here $\mathbf{q}=(q,\phi_q)$ is the electron–hole relative momentum in polar coordinates. The eigenfunctions can be expressed as $\varphi_{\mathbf{q}}=\varphi_q e^{im\phi_q}$, where m is the azimuthal quantum number. The effective Coulomb potential $V_q(z)$ is obtained by solving the Poisson equation for a point charge placed at $z=0$ in the dielectric environment:

$$\varepsilon(z)=\begin{cases}\varepsilon_0\varepsilon_{air} & z>\frac{1}{2}d_{WSe_2}+d_{gap}+d_{WS_2} \\ \varepsilon_0\varepsilon_{WS_2} & \frac{1}{2}d_{WSe_2}+d_{gap}<z<\frac{1}{2}d_{WSe_2}+d_{gap}+d_{WS_2} \\ \varepsilon_0\varepsilon_{gap} \text{ for } & \frac{1}{2}d_{WSe_2}<z<\frac{1}{2}d_{WSe_2}+d_{gap} \\ \varepsilon_0\varepsilon_{WSe_2} & -\frac{1}{2}d_{WSe_2}<z<\frac{1}{2}d_{WSe_2} \\ \varepsilon_0\varepsilon_{diamond} & z<-\frac{1}{2}d_{WSe_2}\end{cases}$$

We set the effective layer thicknesses $d_{WS_2}=d_{WSe_2}=0.57$ nm and $d_{gap}=0.1\pm0.03$ nm. For the relative permittivities we used $\varepsilon^{\perp}_{WSe_2}=7.5$, $\varepsilon^{\perp}_{WS_2}=6.3$, $\varepsilon^{\parallel}_{WSe_2}=13.36$, $\varepsilon^{\parallel}_{WS_2}=11.75$, $\varepsilon_{diamond}=5$, $\varepsilon_{air}=1$ and $\varepsilon_{gap}=1$ (refs. [34,35]), where we account for the strong anisotropy of the dielectric tensor regarding the in- and out-of-plane direction of the adjacent TMD monolayers (see Supplementary Section 3 for details). The resulting potentials $V_q(z)$ for a test charge at $z=0$ and $z=\frac{1}{2}d_{WSe_2}+d_{gap}+\frac{1}{2}d_{WS_2}$ were used as the intra- and interlayer potentials, respectively. These, as well as the resulting 1s and 2p binding energies and wavefunctions, can be seen in Fig. 2e,f. Although the interlayer exciton 1s–2p transition energy clearly differs from the intralayer resonance, the latter is very similar for the hBN (147±3 meV; ref. [20]) and the WS$_2$ (142±9 meV) cover layer (Supplementary Section 3).

From here, we can calculate the oscillator strengths of the intra- and interlayer excitons as

$$f_{1s,2p}=\frac{2\mu}{\hbar^2}E_{1s,2p}\left|\left\langle\varphi^{1s}\left|\mathbf{r}\cdot\mathbf{e}_{\parallel}\right|\varphi^{2p}\right\rangle\right|^2$$

where $E_{1s,2p}$ is the 1s–2p transition energy and $\mathbf{e}_{\parallel}$ is the polarization of the MIR probe pulse. The oscillator strengths are 0.27 for intralayer excitons and 0.44 for interlayer excitons.

Three-fluid model. To analyse the measured MIR spectra more quantitatively, we apply a phenomenological three-fluid model. This approach describes the pump-induced change of the dielectric response function $\Delta\varepsilon(\omega)=\Delta\varepsilon_1(\omega)+\Delta\sigma_1(\omega)/(\varepsilon_0\omega)$ as follows:

$$\Delta\varepsilon(\omega)=\frac{n_{inter}e^2}{d\varepsilon_0\mu_{inter}}\frac{f^{inter}_{1s,2p}}{\frac{E^2_{inter}}{\hbar^2}-\omega^2-i\omega\Delta_{inter}}+\frac{n_{intra}e^2}{d\varepsilon_0\mu_{intra}}\frac{f^{intra}_{1s,2p}}{\frac{E^2_{intra}}{\hbar^2}-\omega^2-i\omega\Delta_{intra}}$$
$$+\frac{e^2}{d\varepsilon_0\mu_{inter}}\frac{A}{\frac{E^2_{higher}}{\hbar^2}-\omega^2-i\omega\Gamma_{higher}} \quad (2)$$

where e is the electron charge, ε_0 denotes the vacuum permittivity, and $f^{inter}_{1s,2p}$ and $f^{intra}_{1s,2p}$ are the oscillator strengths of the 1s–2p transition in inter- and intralayer excitons calculated above. The first and second terms are Lorentzian resonances representing the 1s–2p line of the inter- and intralayer excitons, respectively. They include the interlayer (intralayer) exciton density n_{inter} (n_{intra}), their resonance energy E_{inter} (E_{intra}) and their linewidth Δ_{inter} (Δ_{intra}). The reduced mass of the interlayer excitons $\mu_{inter}=m_e^{WS_2}m_h^{WSe_2}/(m_e^{WS_2}+m_h^{WSe_2})=0.15m_0$ is determined with the effective electron mass in the conduction band of WS$_2$, $m_e^{WS_2}=0.27m_0$, and the effective hole mass in the valence band of WSe$_2$, $m_h^{WSe_2}=0.36m_0$ (ref. [36]). Here, m_0 is the free electron mass. The effective mass of the intralayer excitons $\mu_{intra}=0.16m_0$ is determined with the electron and hole effective masses within the WSe$_2$ monolayer only[36]. The thickness of the sample (treated as a thin slab in this model) is set to $d=0.7$ nm (ref. [19]). The third term in equation (2) phenomenologically models all transitions between higher excited e–h pair states with an effective Lorentzian featuring a resonance energy of $E_{higher}=4$ meV, and an effective scattering rate Γ_{higher}. The parameter $A=n_{higher}f_{higher}$ may be interpreted as an average density n_{higher} of excited-state bound and unbound e–h pairs weighted by a mean oscillator strength f_{higher}. As shown in ref. [30], excited-state transitions in excitons and unbound e–h pairs are indeed expected to occur below the photon energy of our MIR probe pulses. To restrict the number of adjustable parameters, we include all information known a priori: the 1s–2p transition energies of the intra- and interlayer excitons are kept at the values found in Fig. 2 (with a maximum allowable variation of 15%), conforming to theory. Similarly, the inter- and intraexcitonic linewidths are kept between 40 and 120 meV (refs. [19,20]) and the excited-state scattering time is set below 200 fs. Strict limits on the possible values of n_{inter}, n_{intra} and A are set by the fact that both independently retrieved spectra $\Delta\sigma_1$ and $\Delta\varepsilon_1$ have to be reproduced simultaneously. Without any further restrictions, the numerical adaptation of the measured spectra yields an overall good fit quality (Supplementary Fig. 4, black dashed curves). The temporal evolution of the fitting parameters is given in Fig. 4a,b and Supplementary Fig. 5.

Microscopic tunnelling model. The model presented here is an extension of the one detailed in ref. [37], in which equations of motion for exciton densities are derived microscopically using density matrix theory[38] and the Heisenberg equation of motion in a second quantization formalism. It contains three main quantities: the intralayer microscopic polarization P, the intralayer exciton density $n_{\mathbf{Q}}^{intra}$ and the interlayer exciton density $n_{\mathbf{Q}}^{inter}$. Here $\mathbf{Q}$ is the electron–hole centre-of-mass momentum. These quantities only describe the 1s K–K states, where the Coulomb-bound electron and hole are both located at the K valley in the Brillouin zone. The higher excitonic states (2s, 3s, 4s and so on) are treated as a single quantity, n^{higher}. The exciton dynamics is described by the equations

$$\partial_tP=\Omega(t)-(\gamma_{rad}^{intra}+\gamma_p^{intra})P \quad (3)$$

$$\partial_tn_{\mathbf{Q}}^{intra}=2\gamma_p^{intra}|P|^2-2\gamma_{rad}^{intra}\delta_{\mathbf{Q}_0}n_{\mathbf{Q}}^{intra}+\partial_tn_{\mathbf{Q}}^{intra}|_p+\partial_tn_{\mathbf{Q}}^{intra}|_T \quad (4)$$

$$\partial_tn_{\mathbf{Q}}^{inter}=-(2\gamma_{rad}^{inter}\delta_{\mathbf{Q}_0}+\gamma_{nonrad}^{inter})n_{\mathbf{Q}}^{inter}+\partial_tn_{\mathbf{Q}}^{inter}|_p+\partial_tn_{\mathbf{Q}}^{inter}|_T+\partial_tn_{\mathbf{Q}}^{inter}|_{higher} \quad (5)$$

$$\partial_tn^{higher}=\partial_tn^{higher}|_T+\partial_tn^{higher}|_{higher} \quad (6)$$

In equation (3), P is treated in its rotating frame, while $\Omega(t)$ is the Rabi frequency and describes the exciting optical pulse, which is modelled as a Gaussian with a FWHM of 100 fs. $\gamma_{rad}^{intra}=2.59$ ps^{-1} and $\gamma_p^{intra}=26.6$ ps^{-1} are the radiative and phonon-induced decay rates, respectively[37]. The first describes

the radiative decay of excitons within the light cone. The latter leads to the formation of intralayer excitons as seen in the first term of equation (4). The second term in equation (4) describes the radiative decay of excitons within the light cone. The phonon scattering term $\partial_t n_\mathbf{Q}^{intra}|_p = \sum_\mathbf{Q} (\Gamma_{p,\mathbf{Q}\mathbf{Q}'}^{intra} n_\mathbf{Q}^{intra} - \Gamma_{p,\mathbf{Q}\mathbf{Q}}^{intra} n_\mathbf{Q}^{intra})$ couples intralayer exciton states with different momenta. The two terms in the sum describe in- and out-scattering, respectively, mediated by the intralayer phonon scattering rate $\Gamma_{p,\mathbf{Q}\mathbf{Q}'}^{intra}$, which thermalizes the exciton distribution. Because $\Gamma_{p,\mathbf{Q}\mathbf{Q}'}^{intra}$ is a matrix there is no single way to quantify it as a number. It can, however, be instructive to examine the angle-averaged out-scattering rate $\sum_{Q'} \Gamma_{p,\mathbf{Q}\mathbf{Q}'}^{intra}$, which lies between 40 and 140 ps^{-1}. The last term in equation (4) is the tunnelling term $\partial_t n_\mathbf{Q}^{intra}|_T = \sum_{\mathbf{Q}'} \Gamma_{T,\mathbf{Q}\mathbf{Q}'}^{intra-inter} (n_\mathbf{Q'}^{inter} - (1+\alpha) n_\mathbf{Q}^{intra})$, coupling inter- and intralayer states with different momenta. The angle-averaged out-tunnelling rate $\sum_{Q'} \Gamma_{T,\mathbf{Q}\mathbf{Q}'}^{intra-inter}$ lies between 1.4 and 6.8 ps^{-1}. Finally, the factor

$$\alpha = \frac{\sum_{Q',\mu \neq 1s} \Gamma_{T,0Q'}^{1s-\mu,intra-inter}}{\sum_{Q'} \Gamma_{T,0Q'}^{1s-1s,intra-inter}} = 0.84$$ represents the excitons that tunnel into higher excitonic states.

Equation (5) describes the dynamics of interlayer excitons. The two decay rates in the first term are given by $\gamma_{rad}^{inter} = 1.02 \times 10^{-6}$ ps^{-1} (ref. [37]) and $\gamma_{nonrad}^{inter} = 0.03$ ps^{-1}, where the latter is of phenomenological character. The phonon scattering term $\partial_t n_\mathbf{Q}^{inter}|_p$ has the same form as for the intralayer exciton, with $\sum_{Q'} \Gamma_{p,\mathbf{Q}\mathbf{Q}'}^{inter}$ lying between 6 and 40 ps^{-1}. Tunnelling is described by $\partial_t n_\mathbf{Q}^{inter}|_T = \sum_{\mathbf{Q}'} \Gamma_{T,\mathbf{Q}\mathbf{Q}'}^{intra-inter} (n_\mathbf{Q'}^{intra} - n_\mathbf{Q}^{inter})$ where $\Gamma_{T,\mathbf{Q}\mathbf{Q}'}^{inter-intra} = \Gamma_{T,\mathbf{Q}'\mathbf{Q}}^{intra-inter}$ which makes the 1s tunnelling symmetric.

The final term $\partial_t n_\mathbf{Q}^{inter}|_{higher} = \frac{1}{\tau}(\beta n^{higher} \delta_{\mathbf{Q}0} - (1-\beta) n_\mathbf{Q}^{inter})$ describes the interaction with the higher excitonic states. It relies on the assumption that the higher states scatter down to the 1s light cone with zero momentum on a timescale $\frac{\beta}{\tau}$, where $\tau = 250$ fs. It also includes back scattering into the higher states on a timescale $\frac{1-\beta}{\tau}$. Here, we choose $\beta = \frac{1}{Z}\{\exp[-E_{inter}^{1s,K-K}/(k_B T)] + \exp[-E_{inter}^{1s,K-K'}/(k_B T)] + \exp[-E_{inter}^{1s,K-\Lambda}/(k_B T)]\} = 0.57$ where T is the temperature, k_B is the Boltzmann constant and Z is the canonical partition function. By doing this, it is ensured that the system will enter a Boltzmann distribution at equilibrium. Here, the K–K′ and K–Λ states have been taken into account as well. This is motivated by our calculations of the binding energies revealing that the 1s–2p transition energy differs by less than 1 meV from that of the K–K state.

Finally, equation (6) describes the dynamics of higher excitonic states. The first term $\partial_t n^{higher}|_T = \alpha \sum_{\mathbf{Q}\mathbf{Q}'} \Gamma_{T,\mathbf{Q}\mathbf{Q}'}^{inter-intra} n_\mathbf{Q}^{intra}$ describes tunnelling from the intralayer into interlayer excitons. The second term $\partial_t n^{higher}|_{higher} = \frac{1}{\tau}\left((1-\beta)\sum_\mathbf{Q} n_\mathbf{Q}^{inter} - \beta n^{higher}\right)$ handles the interaction with the 1s interlayer state.

To reproduce the densities shown in Fig. 4a,b we integrate over all momenta. Hence we find $n_{inter} = 0.90 \sum_\mathbf{Q} n_\mathbf{Q}^{inter}$, where the factor 0.90 compensates for bleaching from the 2p states assuming a Boltzmann distribution. The corresponding factor for the intralayer excitons is considerably closer to 1.

In this model, only the tunnelling rate is affected by twisting[37]. In the case of a twist angle of 27°, the energy-allowed momentum transfers for the K–K transition lie close to those for the K–K′ and K–Λ transitions. As a result the $\sum_{Q'} \Gamma_{T,\mathbf{Q}\mathbf{Q}'}^{inter-intra}$ rate for 27° ends up between 0.2 and 0.9 ps^{-1}.

Estimate of moiré confinement. Here we introduce a perturbative treatment to approximate the influence of the periodic modulation of the potential landscape induced by the moiré pattern. Therefore, we solve the Schrödinger equation in polar coordinates r and φ assuming a circular finite potential well, meaning that

$$V(r) = \begin{cases} 0, & r \leq r_0 \\ V_0, & r > r_0 \end{cases}$$

For $V(r)$ we have chosen $V_0 = 0.1$ eV and $r_0 = 0.33 a_m$, where $a_m = 3.4$ nm is the moiré period for a stacking angle of $\theta = 5°$ (ref. [39]). Assuming the wavefunctions ψ to be separable in r and φ, we find the (unnormalized) bound-state solutions

$$\psi_{nm}(r,\varphi) = \begin{cases} J_m(k_+ r) e^{im\varphi}, & r \leq r_0 \\ \frac{J_m(k_+ r_0)}{K_m(k_- r_0)} K_m(k_- r) e^{im\varphi}, & r > r_0 \end{cases}$$

where $k_+ = \sqrt{\frac{2\mu}{\hbar^2} E_n}$ outside and $k_- = \sqrt{\frac{2\mu}{\hbar^2}(V_0 - E_n)}$ inside the potential well. The azimuthal quantum number is given by m, and J_m and K_m are the normal and modified Bessel functions of the first and second kinds. In the interval $0 \leq E_n \leq V_0$, n denotes the nth solution to the equation:

$$E_n - \frac{V_0}{1 + \left(\frac{K_m(k_- r_0)(J_{m-1}(k_+ r_0) - J_{m+1}(k_+ r_0))}{J_m(k_+ r_0)(K_{m-1}(k_- r_0) - K_{m+1}(k_- r_0))}\right)} = 0$$

The corresponding binding energy for the 1s state is $E_{1s} = 20$ meV, whereas the shallow troughs of the potential energy landscape do not confine the 2p state. This scenario is expected to result in a transition energy of $E_{2p} - E_{1s} = 20$ meV. Adding this solution to the unperturbed 1s–2p transition energy of the interlayer excitons of 67 meV describes the observed blueshift of the resonance energy by 20 meV.

Data availability
The data sets generated during and/or analysed during the current study are available from the corresponding author upon reasonable request.

References
31. Castellanos-Gomez, A. et al. Deterministic transfer of two-dimensional materials by all-dry viscoelastic stamping. *2D Mater.* **1**, 011002 (2014).
32. Leandro, M. et al. Observation of intense second harmonic generation from MoS$_2$ atomic crystals. *Phys. Rev. B* **87**, 201401 (2014).
33. Berghäuser, G. et al. Mapping of the dark exciton landscape in transition metal dichalcogenides. *Phys. Rev. B* **98**, 020301 (2018).
34. Laturia, A., Van de Put, M. & Vandenberghe, W. Dielectric properties of hexagonal boron nitride and transition metal dichalcogenides: from monolayer to bulk. *NPJ 2D Mater. Appl.* **2**, 6 (2018).
35. Berkelbach, T., Hybertsen, M. & Reichman, D. Theory of neutral and charged excitons in monolayer transition dichalcogenides. *Phys. Rev. B* **88**, 045318 (2013).
36. Kormányos, A. et al. k·p theory for two-dimensional transition metal dichalcogenide semiconductors. *2D Mater.* **2**, 022001 (2015).
37. Ovesen, S. et al. Interlayer exciton dynamics in van der Waals heterostructures. *Commun. Phys.* **2**, 23 (2019).
38. Selig, M. et al. Dark and bright exciton formation, thermalization, and photoluminescence in monolayer transtion metal dichalcogenides. *2D Mater.* **5**, 035017 (2018).
39. Yankowitz, M. et al. Emergence of superlattice Dirac points in graphene on hexagonal boron nitride. *Nat. Phys.* **8**, 382–386 (2012).